Nematic liquid crystals in a spatially step-wise magnetic field

Gaetano Napoli* and Michele Scaraggi†

Dipartimento di Ingegneria dell'Innovazione, Università del Salento, via per Monteroni, Edificio "Corpo O", 73100 Lecce, Italy

(Received 23 July 2015; revised manuscript received 1 October 2015; published 6 January 2016)

We study the molecular reorientation induced by a textured external field in a nematic liquid crystal (nLC). In particular, we consider an infinitely wide cell with strong planar anchoring boundary conditions, subjected to a spatially periodic piecewise magnetic field. In the framework of the Frank's continuum theory, we use the perturbation analysis to study in detail the field-induced splay-bend Fréedericksz transition. A numerical approach, based on the finite differences method, is instead employed to solve the fully nonlinear equations. At high field strengths, an analytic approach allows us to draw the bulk profile of the director in terms of elliptic integrals. Finally, through the application of the Bruggeman texture hydrodynamics theory, we qualitatively discuss on the LCs piecewise director configuration under sliding interfaces, which can be adopted to actively regulate friction. Our study opens the pathway for the application of highly controlled nLC texturing for tribotronics.

DOI: 10.1103/PhysRevE.93.012701

I. INTRODUCTION

Nematic liquid crystals (nLC) are aggregates of rod-like molecules. These molecules have random positions but are averagely aligned along a direction called nematic director **n**. The particular shape and structure make the molecules very sensitive to the presence of electric or magnetic fields. Depending on their dielectric or diamagnetic properties, the molecules reorient along or normally to the direction of the field. Thus, the optical response of a cell containing nematics, which is related to the director orientation, can be driven by the action of external fields. The controllable long range orientational response of nematics is crucial in designing of electro-optic devices, and may contribute as well to the development of a pioneering tribotronic concept in the near future [1–4] (see also in the following).

In the typical configuration of the most wide-spread application, thin layers of a nematic are confined between two flat parallel substrates. The delimiting walls are treated suitably to assign the orientation of the molecules on the boundaries. The condition where the average molecular orientation on the boundary is orthogonal to the delimiting surfaces is called *homeotropic* anchoring. The anchoring is called *planar* when the molecular directors are constrained to lie parallel to the boundary. According to the Oseen-Zocher-Frank theory [5,6], a local stored energy function depending on **n** and $\nabla\mathbf{n}$ is assumed. In the absence of an external field, the director **n** adjusts throughout the sample in order to minimize that energy according to the boundary conditions. In the presence of an external field the nematic tends to align its molecules along or normal to the direction of the field, depending on the dielectric and diamagnetic properties of the molecules. Thus, when a nematic is subjected to an electric field, the free-energy functional shows a further term that takes into account the interaction energy with the applied field.

We consider a nLC sample that is initially in a planar homogeneous alignment. It is well known that if a magnetic field is applied perpendicular to the plates a distortion of the nematic alignment occurs above a critical field strength, provided the magnetic anisotropy is positive. This effect is due to a competition between the restoring elastic forces induced by the alignment at the boundaries, and the destabilizing torques produced by the external field. Below the critical field strength the destabilizing torques are insufficient to overcome the elastic forces and the director profile remains uniform. On the contrary, above this critical field strength the torques overcome the elastic forces and the director profile becomes distorted. This phenomenon is commonly known as a Fréedericksz transition.

Usually the profile distortion changes along the thickness while it remains unchanged along the other directions. Thus, the related problem is a one-dimensional boundary value problem. We observe, however, that inhomogeneous distortions along the boundary direction can arise due to the elastic anisotropy [7–11] or to the weakness of the boundary anchoring [12]. Periodicity can also be induced by variations of the strength of the boundary anchoring [13]. Inhomogeneous distortions in the plane or in the space naturally lead to boundary value problems involving partial derivative equations.

In our case, we deal with a two-dimensional problem where the director distortion is inhomogeneous in the plane spanned by the field direction and the anchoring direction. In particular, the nonuniformity along the anchoring direction is expected to be produced by a *textured external field*, crossing the nematic sample, i.e., a magnetic field applied piecewise along the longitudinal direction of the cell. Although only static distortions are concerned, our analysis is closely inspired by the potential applications of nematics in wet sliding interfaces [1,4], where a piecewise nonuniformity of the director along the anchoring direction, at the microscale, may promote the creation of an active interfacial viscosity micropatterning [1].

While it is already experimentally well-stated that the LCs molecular orientation in a Couette flow can be controlled upon application of electric field [14–16] (supporting the adoption of LCs for the active control of friction), on the other hand lubrication theories for nematic liquid crystals (see, e.g., Ref. [17]) are usually based on assumptions that may become unphysical for realistic interactions, such as neglecting the variation of the director in the direction of

*gaetano.napoli@unisalento.it
†michele.scaraggi@unisalento.it

the flow. On the contrary, we show in the following that this hypothesis fails even qualitatively whenever the external field is applied on a delimited region, rather than on the whole sample, justifying the urgency of this study prior to any further development of the LC lubrication theory and related assumptions. Indeed, at the borderline between regions where the externally applied field undergoes a discontinuity, significant values of the director gradient are obtained. This should be carefully taken into account in a coherent theory of lubrication that involves nematics, and which will be presented in a dedicated contribution.

The manuscript is organized as follows. In Sec. II we formulate the boundary value problem relative to the nLC texturing problem under investigation. In Sec. III we perform a perturbation analysis of the equilibrium equation in order to assess the Fréedericks threshold and the director profile just above the critical field. The numerical and analytical study of the bulk profile in the nonlinear regime are presented and discussed in Sec. IV. In Sec. V we present for the first time the application of LCs in a very simple microtextured tribotronic concept, characterized by a controllable optimal friction. Finally, the conclusions follow in Sec. VI.

II. EQUILIBRIUM EQUATIONS

In our analysis, the nematic occupies the spatial region between two parallel planes placed at $z = 0$ and $z = d$, respectively. We assume strong anchoring boundary condition with $\mathbf{n}$ at the boundary pointing along the x axis; see Fig. 1. The bend-splay geometry is assumed here for simplicity; i.e., the director can only rotate in the x-z plane, thus we can adopt the parametrization $\mathbf{n}(x,z) = \cos[\theta(x,z)]\mathbf{e}_x + \sin[\theta(x,z)]\mathbf{e}_z$, where θ is the angle between the x axis and the director.

We consider that the entire domain consists in an infinity of adjacent identical boxes of infinite length along the y axis, of width L and thickness d. Inside each cell, an external uniform magnetic field of strength H acts orthogonally to the boundaries on regions of length $\bar{x}$, where $0 < \bar{x} \leqslant L$, while in the complementary part of the cell no external field is applied. Thus, we can study the reduced problem on a single planar cell that occupies the region $\{(x,z)|0 \leqslant x \leqslant L, 0 \leqslant z \leqslant d\}$. The magnetic field acts in the region $\{(x,z)|0 \leqslant x \leqslant \bar{x}, 0 \leqslant z \leqslant d\}$.

Assuming the one-constant approximation, the Frank's free energy (per unit of length) becomes

$$2W_F = \int_0^d dz \int_0^L dx\, K|\nabla\theta|^2,$$

where K is a positive parameter. This energy, together with planar strong anchoring, sustains the alignment of the director along the x axis. The field-nematic interaction is instead further described by the term

$$2W_I = -\int_0^d dz \int_0^{\bar{x}} dx\, \chi_a H^2 \sin^2\theta.$$

The constant χ_a measures the difference between the magnetic susceptibility parallel to the director and perpendicular to the director. W_I promotes the alignment of the director in the direction of the field or orthogonally, depending on the sign of χ_a. Here, we assume $\chi_a > 0$, in order to induce a competition between the elastic energy and the magnetic field.

The equilibrium equations are stationary points of the total free-energy functional

$$2W = \int_0^d dz \int_0^L dx[K|\nabla\theta|^2 - \chi_a h(\bar{x} - x)H^2 \sin^2\theta], \quad (1)$$

where $h(\cdot)$ represents the Heaviside step function. The unknown θ satisfies the planar strong anchoring boundary conditions

$$\theta(x,0) = \theta(x,d) = 0, \quad (2)$$

and the periodic boundary conditions

$$\theta(0,z) = \theta(L,z), \quad \partial_x\theta(0,z) = \partial_x\theta(L,z). \quad (3)$$

According to the variational calculus, the Euler-Lagrange equation associated with the functional Eq. (1) is

$$2K\Delta\theta + \chi_a h(\bar{x} - x)H^2 \sin 2\theta = 0. \quad (4)$$

The previous equation, together with the above boundary conditions, always admits the trivial solution $\theta(x,z) = 0$ everywhere. In the next section, we study the field-induced bifurcation from this ground state. However, in the usual applications, the field is applied on the entire sample. This allows us, in the majority of cases, to consider the solution independent of x and, hence, to solve a boundary value problem involving an ordinary differential equation. In such a case, the linear analysis leads to the critical threshold $H_{cr} = (\pi/d)\sqrt{K/\chi_a}$. On the contrary, due to the nonuniformity of the field, in our case the director profile depends on x, and hence the equilibrium problem involves partial differential equations.

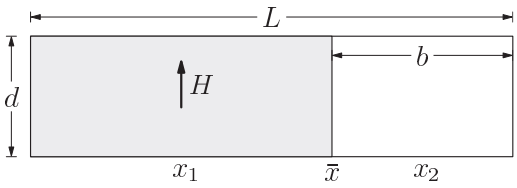

FIG. 1. Schematic representation of the nematic cell.

III. PERTURBATION ANALYSIS

Let us introduce $\xi := \sqrt{\chi_a H^2/K}$, which represents the inverse of the magnetic coherence length. It is a measure for the relevance of the competing field torque versus the elastic restoring effect. The equations to solve become the nonlinear equation

$$2\Delta\theta + \xi^2 \sin 2\theta = 0, \quad 0 \leqslant x \leqslant \bar{x},\ 0 \leqslant z \leqslant d, \quad (5)$$

and the Laplace equation

$$\Delta\theta = 0, \quad \bar{x} \leqslant x \leqslant L,\ 0 \leqslant z \leqslant d. \quad (6)$$

In addition, variational arguments allow us to assume the continuity of θ and of its normal derivative

at $x = \bar{x}$:

$$\lim_{x\to\bar{x}^-} \theta(\bar{x},z) = \lim_{x\to\bar{x}^+} \theta(\bar{x},z),$$
$$\lim_{x\to\bar{x}^-} \partial_x\theta(\bar{x},z) = \lim_{x\to\bar{x}^+} \partial_x\theta(\bar{x},z).$$

In order to assess the critical threshold ξ_{cr}, we consider small perturbations of the undistorted profile. Thus, in what follows, we assume that

$$\epsilon = \sqrt{(\xi - \xi_{cr})/\xi_{cr}} \ll 1 \tag{8}$$

and consider the leading term of the expansion of the solution power series of ϵ:

$$\theta(x,z) = \epsilon\vartheta(x,z) + o(\epsilon).$$

Then we substitute it into Eq. (5) and into the boundary conditions. Up to the first order, we have to solve the linear system of partial differential equations:

$$\Delta\vartheta + \xi_{cr}^2\vartheta = 0, \quad 0 \leqslant x \leqslant \bar{x},\ 0 \leqslant z \leqslant d, \tag{9a}$$
$$\Delta\vartheta = 0, \quad \bar{x} \leqslant x \leqslant L,\ 0 \leqslant z \leqslant d, \tag{9b}$$

together with the boundary conditions

$$\vartheta(x,0) = \vartheta(x,d) = 0, \tag{10}$$

with the periodic conditions

$$\vartheta(0,z) = \vartheta(L,z), \quad \partial_x\vartheta(0,z) = \partial_x\vartheta(L,z), \tag{11}$$

and with the continuity conditions at $x = \bar{x}$,

$$\lim_{x\to\bar{x}^-} \vartheta(\bar{x},z) = \lim_{x\to\bar{x}^+} \vartheta(\bar{x},z), \tag{12a}$$
$$\lim_{x\to\bar{x}^-} \partial_x\vartheta(\bar{x},z) = \lim_{x\to\bar{x}^+} \partial_x\vartheta(\bar{x},z). \tag{12b}$$

Let us start by considering solutions in the region where the magnetic file is applied. We look for solutions [Eq. (9a)] of the kind $\vartheta(x,z) = \mathcal{X}(x)\mathcal{Z}(z)$. Thus, we arrive to

$$\partial_{xx}\mathcal{X}\mathcal{Z} + \mathcal{X}\partial_{zz}\mathcal{Z} + \xi_{cr}^2\mathcal{X}\mathcal{Z} = 0,$$

which can be split into two ordinary differential equations:

$$\partial_{xx}\mathcal{X} + \left(\xi_{cr}^2 - \lambda^2\right)\mathcal{X} = 0, \quad \partial_{zz}\mathcal{Z} + \lambda^2\mathcal{Z} = 0. \tag{13}$$

In particular, $\mathcal{Z}$ satisfies the homogeneous boundary conditions $\mathcal{Z}(0) = \mathcal{Z}(d) = 0$ and, therefore, it can be expressed as a sine Fourier series, whose nth mode is

$$\mathcal{Z}_n = \sin(\lambda_n z), \quad \lambda_n = \frac{n\pi}{d},$$

which already satisfies the boundary conditions Eq. (10). By substituting λ_n into Eq. (13), we obtain

$$\partial_{xx}\mathcal{X}_n + \omega_n^2\mathcal{X}_n = 0,$$

where $\omega_n^2 = \xi^2 - \lambda_n^2$, and hence

$$\mathcal{X}_n = a_n\cos[\omega_n(x - x_1)] + b_n\sin[\omega_n(x - x_1)], \tag{14}$$

with $0 \leqslant x \leqslant \bar{x}$, where we have set $x_1 = \bar{x}/2$. The quantity ω_n, and hence ξ_{cr}, can be determined once imposing the periodicity and the continuity conditions at $x = \bar{x}$.

In a similar way, in the region where no external field is applied, we look for solutions of the kind $\vartheta(x,z) = \tilde{\mathcal{X}}(x)\tilde{\mathcal{Z}}(z)$ and we arrive to

$$\tilde{\mathcal{Z}}_n = \sin(\lambda_n z), \tag{15}$$

$$\tilde{\mathcal{X}}_n = a_n\cosh[\lambda_n(x - x_2)] + d_n\sinh[\lambda_n(x - x_2)], \tag{16}$$

with $\bar{x} \leqslant x \leqslant L$, where $x_2 = \bar{x} + (L - \bar{x})/2$. It is worth noticing that, since λ_n is a real number, $\tilde{\mathcal{X}}_n$ can be written in term of only hyperbolic sines and cosines. On the contrary, the $\mathcal{X}_n$ can be described in terms of trigonometric functions or in terms of hyperbolic functions as well, since the sign of ω_n^2 cannot be *a priori* established.

According to Eqs. (11) and (12), the obtained solutions must satisfy the linear conditions

$$\mathcal{X}_n(\bar{x}) = \tilde{\mathcal{X}}_n(\bar{x}), \quad \partial_x\mathcal{X}_n(\bar{x}) = \partial_x\tilde{\mathcal{X}}_n(\bar{x}), \tag{17a}$$
$$\mathcal{X}_n(0) = \tilde{\mathcal{X}}_n(L), \quad \partial_x\mathcal{X}_n(0) = \partial_x\tilde{\mathcal{X}}_n(L). \tag{17b}$$

These conditions lead to an homogeneous system of linear equations, with unknowns a_n, b_n, c_n, and d_n, where nontrivial solutions are allowed if and only if the matrix of the coefficients M_n is singular.

Let us denote $j_n = \det(M_n)$. A direct inspection shows that j_n can be written as the product of two terms $j_n = j_n^{(e)}j_n^{(o)}$. The term $j_n^{(e)}$ (respectively, $j_n^{(o)}$) represents the determinant of 2×2 matrix obtained considering solutions that in each region have an even (respectively, odd) symmetry with respect to x_1 and x_2. In other words, solutions with even parity corresponds to set $b_n = 0$ and $d_n = 0$; on the contrary, the odd symmetry requires $a_n = 0$ and $c_n = 0$. In particular, we obtain

$$j_n^{(e)} = \omega_n\cosh\left(\frac{b}{2}\lambda_n\right)\sin\left(\frac{\bar{x}}{2}\omega_n\right) - \lambda_n\sinh\left(\frac{b}{2}\lambda_n\right)\cos\left(\frac{\bar{x}}{2}\omega_n\right), \tag{18a}$$
$$j_n^{(o)} = \lambda_n\cosh\left(\frac{b}{2}\lambda_n\right)\sin\left(\frac{\bar{x}}{2}\omega_n\right) + \omega_n\sinh\left(\frac{b}{2}\lambda_n\right)\cos\left(\frac{\bar{x}}{2}\omega_n\right), \tag{18b}$$

where $b = L - \bar{x}$. To make M_n singular it is sufficient that only one of two terms vanishes. This means that the bifurcation originates with a given symmetry of the director profile. Thus, on one side, equation $j_n = 0$ allows us to determine the critical threshold of the bifurcation. On the other side, depending on the critical threshold being a root of $j_n^{(e)} = 0$ or of $j_n^{(o)} = 0$, we can have a solution with even or odd symmetry, respectively.

A. The critical threshold

Hereinafter, we collect some analytical properties of the equation $j_n = 0$. We start by observing that $\omega_n = 0$, and therefore $\xi_{cr} = n\pi/d$, is always solution of $j_n^{(o)} = 0$. Nevertheless, these solutions yield $\vartheta = 0$, and hence they must be discarded because they do not produce a buckling.

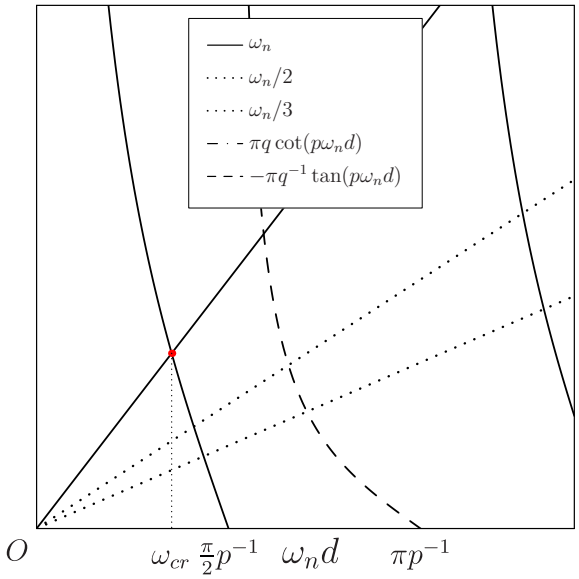

FIG. 2. Qualitative behavior of the roots of the threshold equation $j = 0$.

In any case, the equation $j_n = 0$ is an implicit equation involving the mode number n and the two aspect ratio $\ell := \bar{x}/d$ and $\beta := b/d$, where $\ell + \beta = L/d$. Obviously, since ω_n is an increasing function of $\xi_{\rm cr}$, the critical threshold is expected in correspondence of the lowest ω_n.

We now demonstrate that ω_n attends it minimum for $n = 1$. Indeed, whenever β and ℓ are fixed, the equations $j_n^{(e)} = 0$ and $j_n^{(0)} = 0$ can be recast in the form

$$n^{-1}\omega_n d = \pi q \cot(p\ \omega_n d), \tag{19a}$$

$$n^{-1}\omega_n d = -\pi q^{-1}\tan(p\ \omega_n d), \tag{19b}$$

respectively, where q ad p are positive constants. The right-hand sides of both Eqs. (19), which do not depend explicitly on n, consist in two decreasing functions of ω_n (the dashed and dash-dotted lines in Fig. 2). On the contrary, the left-hand side represents straight lines of slope $1/n$. As shown in Fig. 2, the lowest root is determined by the intersection between the highest slope straight line ($n = 1$) and the dash-dotted curve.

Furthermore, Fig. 2 sketches how the lowest root of Eq. (19a) is expected in the interval $0 < \omega_1 d < \frac{\pi}{2}p^{-1}$, while the lowest root of Eq. (19b) (apart $\omega_1 = 0$, which must be discarded for the reasons reported above) falls in the range $\frac{\pi}{2}p^{-1} < \omega_1 d < \pi p^{-1}$. In conclusion, we can assert that the critical threshold is the lowest solution of $j_1^{(e)} = 0$ and, consequently, the buckled solution exhibits an even symmetry with respect to $x = x_1$ and $x = x_2$, consisting to set $b_1 = 0$ and $d_1 = 0$ in Eqs. (14) and (16), respectively. A schematic representation of the director field is portrayed in Fig. 3.

Figure 4 reports on the lowest solution of Eqs. (18a) (solid lines) and (18b) (dashed lined) for several values of the ratio $\bar{x}/L$. This figure confirms that $\omega_{\rm cr}$ is obtained as solution of Eq. (18a). Furthermore, as expected, the critical threshold is a deceasing function of $\bar{x}/L$.

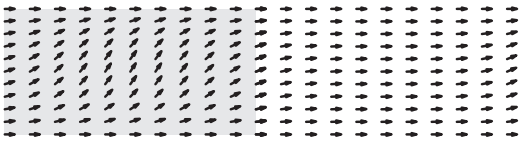

FIG. 3. Schematic representation of the post-buckling director alignment. The vertical external field is applied in the shaded region.

By analyzing Eq. (18a), we discover that the critical threshold shows two behavior regimes:

(i) Whenever $\bar{x}$ approaches L, i.e., for tiny values of β, Eq. (18a) is dominated by the hyperbolic functions. In this regime, we obtain

$$\omega_{\rm cr} \approx \frac{\pi}{d}\sqrt{1 - \frac{\bar{x}}{L}}. \tag{20}$$

In the special case whenever $\bar{x} = L$, one obtains $\omega_{\rm cr} = 0$ and therefore $\xi_{\rm cr} = \pi/d$, corresponding to the classical result $H_{\rm cr} = (\pi/d)\sqrt{K/\chi_a}$.

(ii) On the contrary, as $\pi\beta/2$ becomes $O(1)$, the contribution of the hyperbolic functions becomes negligible. In this regime, we look for solutions with $\omega_1\bar{x} \ll 1$ and we find

$$\omega_{\rm cr} \approx \frac{2\sqrt{3\pi}}{\sqrt{\bar{x}(\pi\bar{x} + 6d)}}. \tag{21}$$

Figure 5 shows the comparison between the numerical (see in the following) and the analytical solutions throughout the entire interval $0 < \bar{x} \leqslant L$.

B. Amplitude determination

Until now, we can state that the post buckling solution involves the first Fourier mode in the z direction, that is $n = 1$, showing an even symmetry with respect to $x = x_1$ and $x = x_2$. Thus, we have

$$\theta = \epsilon a_1 \cos\left[\omega_{\rm cr}(x - x_1)\right]\sin\left(\frac{\pi}{d}z\right) \quad 0 \leqslant x \leqslant \bar{x}, \tag{22a}$$

$$\theta = \epsilon c_1 \cosh\left[\frac{\pi}{d}(x - x_2)\right]\sin\left(\frac{\pi}{d}z\right) \quad \bar{x} \leqslant x \leqslant L. \tag{22b}$$

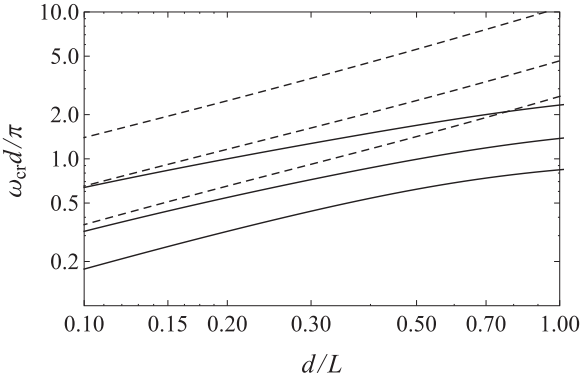

FIG. 4. $\omega_{\rm cr}d/\pi$, solution of Eqs. (18a) (solid lines) and (18b) (dashed lines) as a function of the aspect ratio d/L, for $\bar{x}/L = 0.1$, 0.25, and 0.5 (from top to bottom).

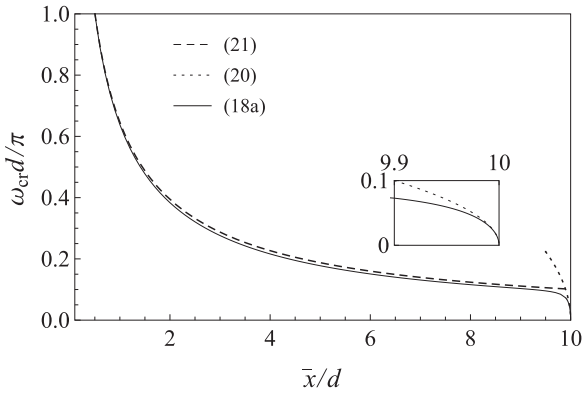

FIG. 5. Numerical solution of Eq. (18a) (with $L/d = 10$) compared with the analytical approximated solution Eqs. (20) and (21). The inset represents the magnification of the region close to $\bar{x}/d = 10$.

In addition, one of the conditions, Eq. (17), can be used to obtain $c_1 = a_1 \cos(\omega_{cr}\bar{x}/2)/\cosh[(b\pi)/(2d)]$. However, up to this point, the solution to the linear problem is incomplete, since its amplitude a_1 remains undetermined. In order to assess the profile amplitude ϵa_1, fourth-order terms in the energy expansion are retained [18]. We substitute Eqs. (22) and (8) into Eq. (1), obtaining, up to the fourth order,

$$W = \epsilon^2 W^{(2)} + \epsilon^4 W^{(4)},$$

where

$$W^{(2)} = -a_1^2 d \cos\left(\frac{\omega_{cr}}{2}\bar{x}\right)\mathrm{sech}\left(\frac{\pi b}{2d}\right) j_1^{(e)},$$

which vanishes at the critical threshold, and

$$W^{(4)} = -\frac{d\xi_{cr}}{2\omega_{cr}}\left\{[\omega_{cr}\bar{x} + \sin(\omega_{cr}\bar{x})]a_1^2 - [6\omega_{cr}\bar{x} + 8\sin(\omega_{cr}\bar{x}) + \sin(2\omega_{cr}\bar{x})]\frac{a_1^4}{64}\right\}.$$

Having performed the integration, it remains to minimize the energy with respect to the amplitude a_1. Thus, we arrive at $a_1 = 0$ and

$$a_1 = \pm\frac{4\sqrt{2}\sqrt{\omega_{cr}\bar{x} + \sin(\omega_{cr}\bar{x})}}{\sqrt{6\omega_{cr}\bar{x} + 8\sin(\omega_{cr}\bar{x}) + \sin(2\omega_{cr}\bar{x})}}. \quad (23)$$

The former corresponds to the trivial solution, which becomes unstable beyond the critical threshold. The two opposite solutions correspond to clockwise and counterclockwise rotations of the director. Equation (23) can be approximated by $a_1 = \pm 2 + O(\bar{x}^2\omega_{cr}^2)$.

IV. NUMERICAL RESULTS AND NONLINEAR ANALYSIS

Here we present a numerical approach for the resolution of the fully nonlinear boundary value problem reported above. By introducing the dimensionless variables $Z = z/d$ and $X = x/d$, we first rephrase Eq. (5) in the following dimensionless equation:

$$\Delta\psi + \Xi^2 \sin\psi = 0, \quad (24)$$

where $\psi = 2\theta$, and $\Xi(x) = d\xi$ for $x < \bar{x}$ [$\Xi(x) = 0$ otherwise]. The Laplacian operation is now understood with respect to the dimensionless coordinates.

Then Eq. (24) is discretized on a regular rectangular mesh of size (k_X, k_Z), with grid size (δ_X, δ_Z), by central finite differences, resulting in the following:

$$\psi_{i+1,j} + \psi_{i-1,j} + \delta_X^2/\delta_Z^2(\psi_{i,j+1} + \psi_{i,j-1}) - 2\psi_{i,j}\left(1 + \delta_X^2/\delta_Z^2\right) + \delta_X^2\,\Xi_{ij}^2 \sin\psi_{ij} = L_{ij}, \quad (25)$$

with $L_{ij} = 0$. Equation (25) is linearized in

$$L_{ij}^k = L_{ij}^{k-1} + \left[\frac{\partial L_{ij}}{\partial\psi_{hk}}\right]^{k-1}\Delta\psi_{hk}, \quad (26)$$

where $\partial L_{ij}/\partial\psi_{i+1,j} = \partial L_{ij}/\partial\psi_{i-1,j} = 1$, $\partial L_{ij}/\partial\bar{\theta}_{i,j+1} = \partial L_{ij}/\partial\psi_{i,j-1} = \delta_X^2/\delta_Z^2$,

$$\partial L_{ij}/\partial\psi_{ij} = -2\left(1 + \delta_X^2/\delta_Z^2\right) + \delta_X^2\,\Xi_{ij}^2\cos\psi_{ij},$$

and 0 elsewhere. Periodicity ($i = 1$ and $i = k_X$) and Cauchy conditions ($j = 1$ and $j = k_Z$) are applied on the boundaries. Hence, by imposing $L_{ij}^k = 0$, Eq. (26) can be solved in $\Delta\psi$, and ψ^k iteratively under-relaxed accordingly to $\psi^k = \psi^{k-1} + c\Delta\psi$, where c in the range 0.01 to 0.1 has been adopted in calculations. The iterations are arbitrarily truncated when $|L_{ij}| \to 0$ and $|\psi_{ij}| \to 0$, where $|\cdot|$ is here considered as a suitable numerical norm operator. We observe that while Eq. (25), and the related linearization, can clearly differ depending on the complexity of the rheological description of the LCs (e.g., when including the elastic anisotropy), the iterative resolution scheme is expected not to be affected for static interactions.

As shown before, this boundary value problem admits a nonunique solution. Thus, to promote the convergence of the numerical results toward the solution with the proper symmetry, we used Eq. (22) as a guess solution in the numerical code.

In Figs. 6 and 7 we show for a texture density $\bar{x}/L = 0.2$ and $\bar{x}/L = 0.5$, respectively, the maximum director angle θ_{max} as a function of the dimensionless applied field. Each figure is a branch of a pitchfork bifurcation. The intersection of the curve with the axis $\theta_{max} = 0$ represents the numerical critical threshold [24], which perfectly agrees with the theoretical prediction. For field strengths just below the critical threshold, the value of θ_{max} is well captured by the theoretical analysis done in the previous section. In the strong field regime, we compare the numerical result with the one obtained in Refs. [19,20], that we report here below for ease of reading:

$$\theta_{max} \approx 4\tan^{-1}\left[\tanh\left(\frac{\xi}{4}\right)\right] - \frac{\pi}{2}. \quad (27)$$

However, this formula has been derived within the hypothesis that the external field is applied on the whole domain. Consequently, it works better in the limit of slender cell. This explains the discrepancy between with the numerical results in stocky cells [$\bar{x}/d$ is $O(1)$], where the effects due to the discontinuity of the field become relevant.

Figure 8 reports the profile of θ in the middle of the cell $z = d/2$ for several values of the applied field. The gap between the numerical and the approximate analytical solution Eq. (22) increases as the applied field increases. The plateau region in the numerical solution is well captured by the asymptotic

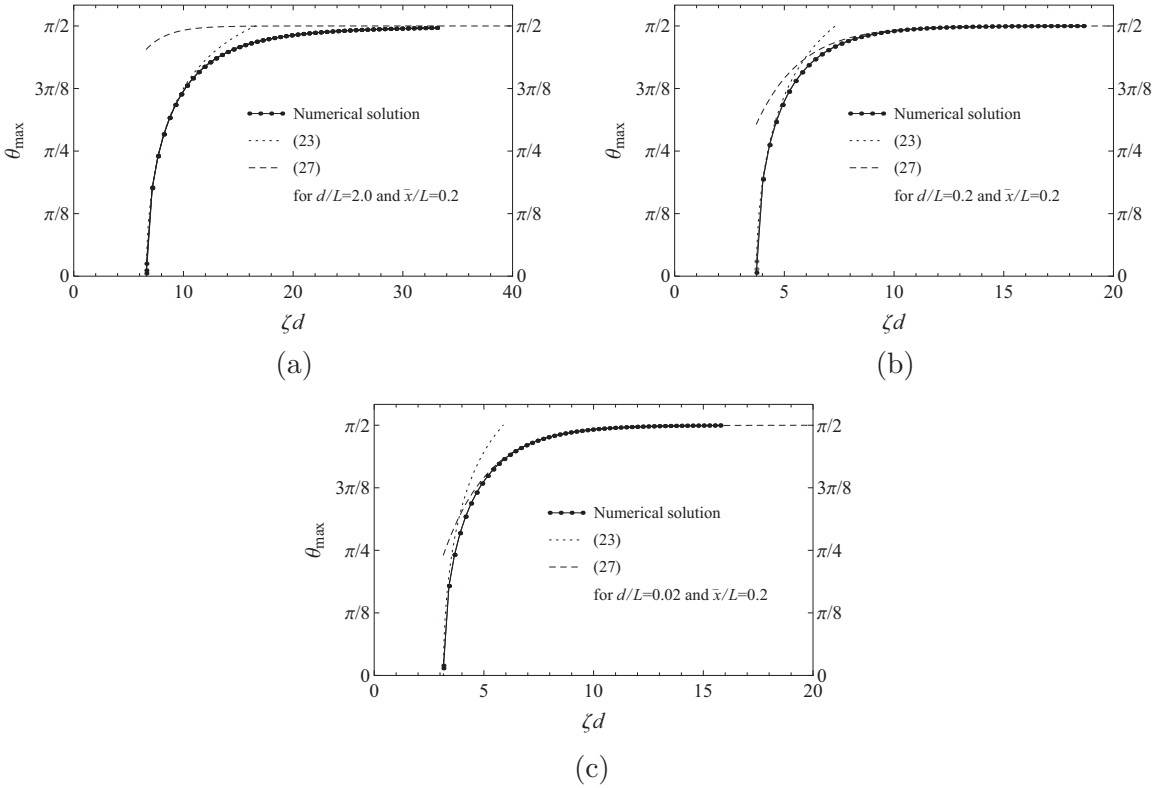

FIG. 6. The predictions of Eqs. (23) and (27) compared with the numerical results, at a constant texture ratio $p_h = \bar{x}/L = 0.2$. For several aspect ratios, (a) $d/L = 2$, (b) $d/L = 0.2$, (c) $d/L = 0.02$.

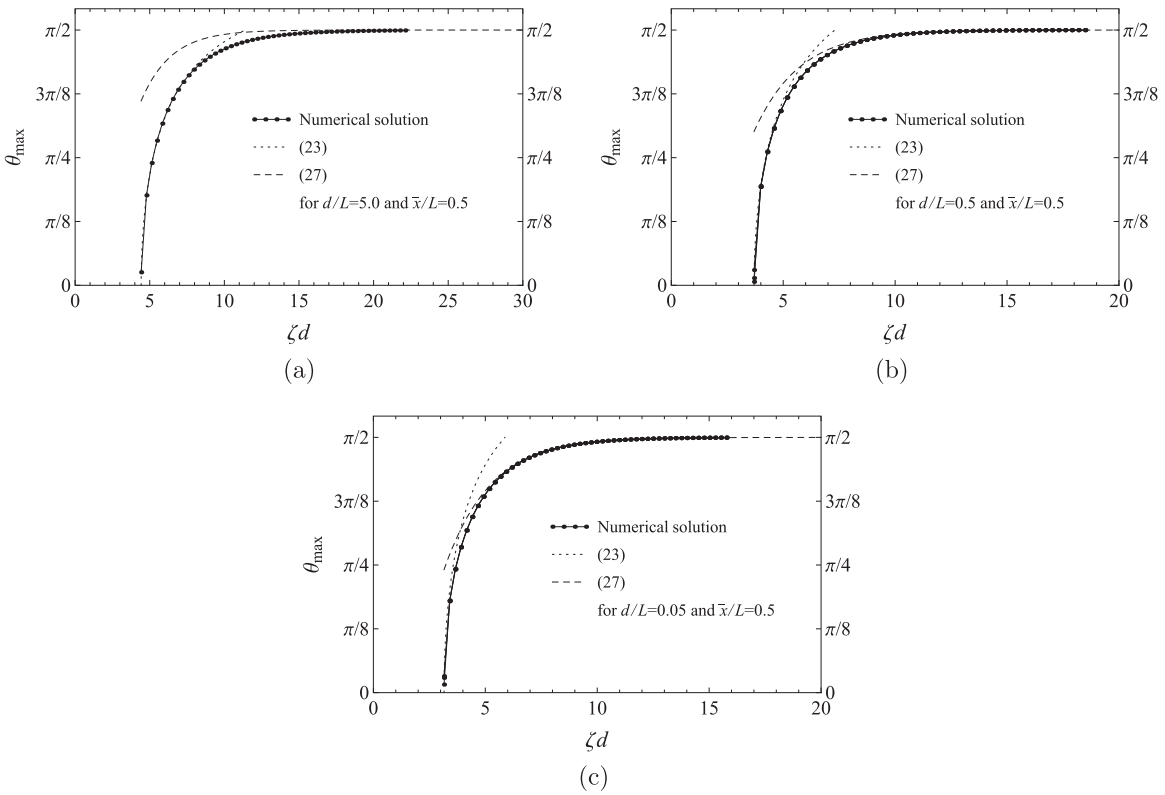

FIG. 7. The predictions of Eqs. (23) and (27) compared with the numerical results, at a constant texture ratio $p_h = \bar{x}/L = 0.5$. For several aspect ratios, (a) $d/L = 5$, (b) $d/L = 0.5$, (c) $d/L = 0.05$.

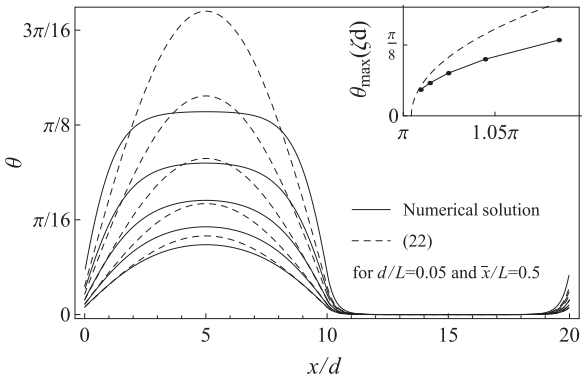

FIG. 8. Profile of θ at $z = d/2$ for several values of the strength field. Comparison between the numerical solutions (solid lines) with the linear analytical solutions Eq. (22) (dashed lines).

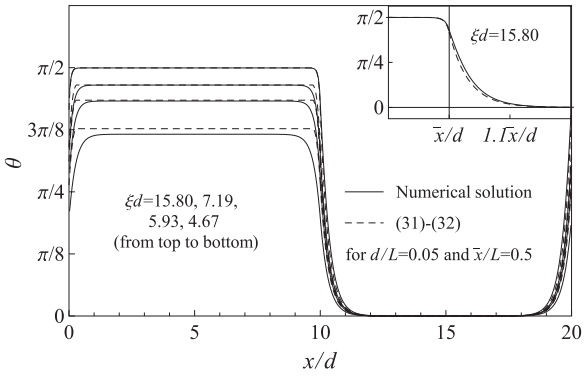

FIG. 9. Profile of θ at $z = d/2$ for several values of the strength field. Comparison between the numerical solutions (solid lines) and the nonlinear solution Eqs. (31) and (32) (dashed lines).

solution Eq. (27). In any case, we notice that the effect of the field decays upon a characteristic length of the order of the cell thickness d.

To assess the analytical behavior of the profile in the middle of the cell, we observe first that at $z = d/2$ the boundary effect can be neglected. Consequently, in a neighborhood of $x = \bar{x}$, we can assume $\partial_{zz}\theta \ll \partial_{xx}\theta$, which allows us to approximate Eq. (5) by

$$2\partial_{xx}\theta + \xi^2 \sin 2\theta = 0, \quad 0 \leqslant x \leqslant \bar{x},\ 0 \leqslant z \leqslant d. \tag{28}$$

This equation looks like the pendulum equation. Thus, we obtain the first integral

$$(\partial_x\theta)^2 + \xi^2 \sin^2\theta = \xi^2 \sin^2\theta_1, \tag{29}$$

where $\theta_1 := \theta(x_1,d/2)$ is the maximum value of $\theta(x,d/2)$. Within the high field regime we can set $\theta_1 = \theta_{\max}$ provided by Eq. (27).

A direct inspection of Eq. (29) yields

$$dx = \pm \frac{d\theta}{\xi\sqrt{\sin^2\theta_1 - \sin^2\theta}}, \tag{30}$$

where the sign $+$ (respectively, $-$) is to be used in the interval $x \in (0,x_1)$ (respectively, $x \in (x_1,\bar{x})$). We focus on the interval $(x_1,\bar{x})$ where integration of Eq. (30) between $\bar{x}$ and x leads to

$$\xi(x - \bar{x}) = \csc\theta_1[\mathrm{F}(\bar{\theta}, \csc^2\theta_1) - \mathrm{F}(\theta, \csc^2\theta_1)], \tag{31}$$

where F denotes the incomplete elliptic integral of first kind and $\bar{\theta} := \theta(\bar{x},d/2)$.

In the region without applied field, θ satisfies the Laplace equation and, hence, we have

$$\theta(x,d/2) = C_1 \cosh\left(\frac{\pi}{d}(x - x_2)\right). \tag{32}$$

Finally, the two arbitrary constants $\bar{\theta}$ and C_1 can be determined by imposing the continuity conditions at $x = \bar{x}$

$$\bar{\theta} = C_1 \cosh\left[\frac{\pi}{d}(\bar{x} - x_2)\right], \tag{33a}$$

$$-\xi\sqrt{\sin^2\theta_1 - \sin^2\bar{\theta}} = C_1\frac{\pi}{d}\sinh\left[\frac{\pi}{d}(\bar{x} - x_2)\right]. \tag{33b}$$

Figure 9 shows the comparison between the numerical solutions and the approximate solutions provided by Eqs. (31)–(33), for several values of the applied field. The bulk approximate solution works better in the regime of high applied fields.

V. DISCUSSION

During the past couple of decades, LCs found several technological applications in electro-optical and electromechanical devices, ranging from the well-known LC displays to liquid crystal thermometers, switchable windows, electro-optical zoom lenses, microvalves, and microdampers, to cite few [15]. One of the largest advantages of electrorheological LCs over other smart fluids (e.g., magnetorheologic fluids, given by microscale particles suspension) is that they are free from suspended heterogeneities, which makes them particularly attractive for for microsystems and microchannels applications, and even more for tribological applications. Among others, the rheological properties of nLCs have been extensively studied at both fundamental and more engineering level. At least for simple kinematics (e.g., Couette flow), nLCs shear viscosity can be easily controlled [21] upon application of external fields such as electric and magnetic fields, which change the orientation of the director (the locally averaged direction of molecules) with respect to the flow velocity. Thus, nLCs with positive dielectric anisotropy (i.e., the dielectric constant parallel to the director $\epsilon_{||}$ is larger than that perpendicular to it, $\epsilon_{\perp}$) confined between sliding plates, show a noticeable increase in the apparent viscosity upon application (perpendicularly to the sliding direction) of an external electric field, due to the alignment of the director along the external field. Inversely, polar molecules with permanent dipole moments may exhibit a negative dielectric anisotropy, resulting in the opposite effect.

This ability to control viscosity through the application of an external field (e.g., electric) makes the investigation of stepwise LC dynamics of extreme interest for the development of a tribotronic discipline. As an example, the ability to locally (at the microscale) manipulate the lubricant flow in sliding contacts has been recently demonstrated [4] to be the pathway for the engineering of surfaces with on-demand contact properties, such as (a constantly reduced) friction. This can be effectively achieved by adopting a textured contact interface, where the texture can be a lattice of surface (i) structural, (ii) slippery, or (iii) *viscosity* defects (or both), i.e., a distribution of inhomogeneities in the local flow conductivity field [1–4].

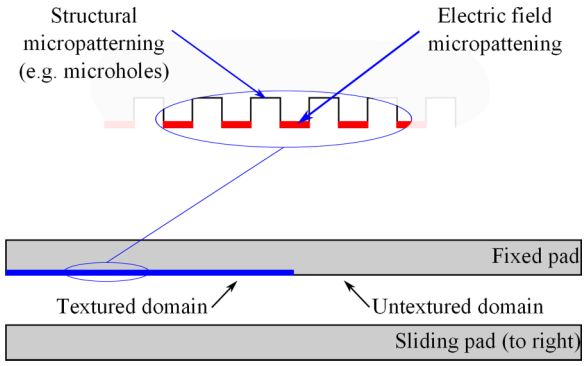

FIG. 10. Schematic of a macroscopic contact pair (assumed, for simplicity, infinitely wide in the out-of-plane direction) in a sliding interaction. Both surfaces are macroscopically smooth; however, the top surface is characterized by a microtexturing on the inlet side. We consider two texture cases, namely (i) a microstructural patterning, constituted by an ordered repetition of microgrooves perpendicular to the sliding direction, and (ii) a microstructural (as before) and microviscosity patterning. In the calculations below we have assumed that the textured side is $1/2$ of the total bearing length, whereas the in-plane size of the generic texture defect is $1/2$ of the patterning lattice. In the BTH theory [1] the viscosity is assumed constant across and along the gap under electrodes, an assumption that is not quite in agreement with the theoretical results provided above.

However, we stress that while the adoption of optimized textured surfaces can result in a remarkable control of the macroscopic contact properties, such as friction, on the other side the optimal contact performances can be achieved only (relatively) closely to the reference operating conditions [4]. Thus, an optimal texture, e.g., minimizing friction at a sliding speed v_1 will not be effective at different sliding velocities, making questionable the adoption of surface texturing for realistic applications. A possible solution for the previous issue would be the active control of the microtexturing of fluid flow conductivities, capable to comply with the varying contact conditions. This can be achieved, e.g., adopting LC-lubricated confined sliding plates with micropatterned electrodes, an active viscosity micropatterning, which is expected to provide a huge step forward to this research field.

In Fig. 10 we illustrate the schematic of a macroscopic contact pair (assumed, for simplicity, infinitely wide in the out-of-plane direction) in a sliding interaction. Both surfaces are macroscopically smooth; however, the top surface is characterized by a microtexturing on the inlet side. We consider two texture cases, namely (i) a microstructural patterning and (ii) a microstructural and microviscosity patterning. The Bruggeman texture hydrodynamics (mean field) theory (BTH [1]) can be applied here to analytically determine the friction and supported normal load for textured interfaces. In particular, we observe first that for such a macroscopic contact geometry (flat-on-flat) a zero load (and, consequently, an infinite friction) would be theoretically predicted in the absence of surface texture.

However, by applying the BTH theory for the structural-only texture (i), the minimum friction $\mu_{\rm opt} = h_0 L_0^{-1}(27 + 33 \times 3^{1/3} + 19 \times 3^{2/3})/8$ is achieved for a groove depth $h_{d,\rm opt} = h_0(-1 + 3^{-1/3} + 3^{1/3})/2$, where h_0 is the nominal

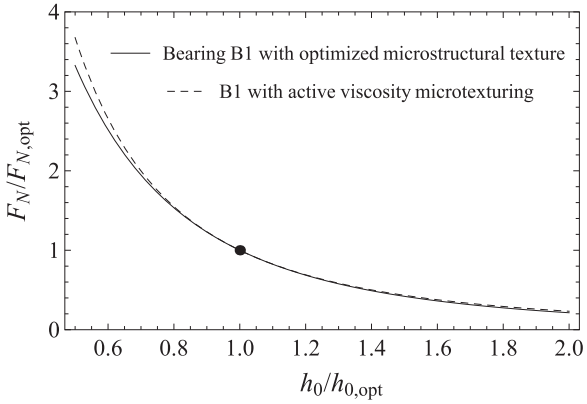

FIG. 11. Normalized load $F_{\rm N}/F_{\rm N,opt}$ as a function of the normalized separation $h_0/h_{0\rm opt}$, for an optimized bearing (i) microstructural patterning (black line) and (ii) microstructural and microviscosity patterning (dashed line).

interface separation. h_0 is related to the normally applied load $F_{\rm N,opt}$ through $F_{\rm N,opt} = \eta v h_0^{-2} L^2 (3^{-1/3} + 3^{1/3} - 2)$, where v is the sliding speed and η the fluid dynamic viscosity (note: $F_{\rm N,opt}$ is a load by length). Thus, for a given $h_{d,\rm opt}$, when increasing (decreasing) the normal load $F_{\rm N}$ with respect to $F_{\rm N,opt}$, the nominal separation h_0 must accordingly decrease (increase) with respect the optimal separation $h_{0\rm opt} = 2h_{\rm d,opt}/(-1 + 3^{-1/3} + 3^{1/3})$. This is shown in Fig. 11 (black curve), whereas the corresponding friction curve $\mu/\mu_{\rm opt}$ as a function of the normalized load $F_{\rm N}/F_{\rm N,opt}$ is reported in Fig. 12 (black curve). Note that, as expected, the friction nonnegligibly increases once the normally applied load is varied from the optimal-design value.

Supported by the results of the static analysis for spatially periodic piecewise external field provided above, here LCs can be adopted with *sliding patterned electrodes* to provide an active control of the microflow dynamics through the generation of a *viscosity patterning* superposed to the microstructural patterning; see, e.g., the schematic of Fig. 10 [case (ii)]. In particular, friction can be kept to the minimum value at varying load conditions (see Fig. 12, dashed curve) by adopting the LCs viscosity as a function of the normalized load reported in Fig. 13, whereas (remarkably) leaving the bearing load curve

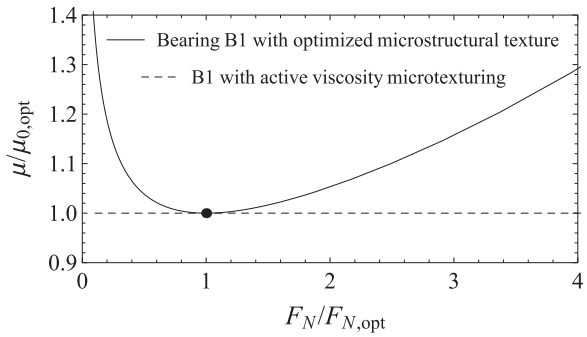

FIG. 12. Normalized friction $F_{\rm N}/F_{\rm N,opt}$ as a function of the normalized separation $h_0/h_{0\rm opt}$, for an optimized bearing (i) microstructural patterning (black line) and (ii) microstructural and microviscosity patterning (dashed line).

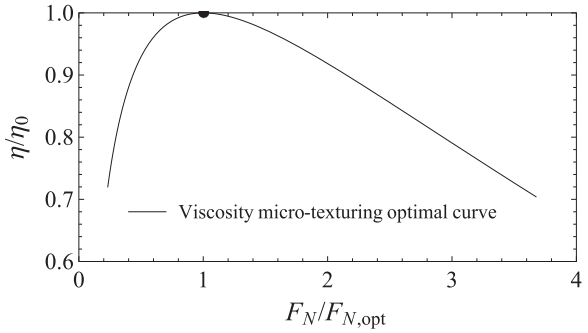

FIG. 13. LCs normalized viscosity (minimizing the sliding friction) as a function of the normalized load, corresponding to the bearing load curve of Fig. 11 (dashed line) and to the friction curve of Fig. 13 (dashed line).

(see Fig. 11, dashed curve) mostly unaffected by the adoption of the viscosity patterning.

In the BTH theory [1] employed above, the viscosity is assumed constant across and along the gap under electrodes, an assumption which seems to fail accordingly to the theoretical results provided in the previous sections. Moreover, we have also showed that the decaying length of the LC director across the stepwise field variation is $\approx h_0$, a phenomenon that is not taken into account in the mean-field lubrication model [1]. However, we observe that while the latter (and in particular the lubrication assumption) has to be reformulated in order to include the mechanisms highlighted above, the stepwise patterning of the LCs apparent viscosity seems to promote a breakthrough in the development of effective smart interfaces with controllable tribological properties, such as friction.

VI. CONCLUDING REMARKS

We have used the Frank's equations to model the static properties of a simple liquid crystal device consisting of a nematic material between two parallel plates whose texture is distorted by the application of a step-wise electric field. This serves as an archetype for more complex but realistic liquid crystal devices of practical importance.

A systematic asymptotic analysis has been applied and solution derived for two different regimes of the dimensionless applied field: close to the Fréedericks threshold and in the high field regime. In particular, we have established the influence of the geometry on the behavior of the critical threshold. Just beyond the threshold, the solutions have a single Fourier mode along z and even periodic symmetry along x. We have also explored the behavior of θ in the center of the cell at $z = d/2$. In this region the z derivative can be neglected and we have shown that the initial sinusoidal buckling profile evolves into a *quasi*-stepwise profile as the field strength is raised. Finally, we have shown through the application of the recent Bruggeman texture hydrodynamics theory to a simple plain bearing geometry that the stepwise micropatterning of the LCs apparent viscosity can be adopted for the development of effective smart interfaces with on-demand tribological properties, such as friction.

We observe that, in view of a reformulation of a lubrication theory in the presence of a textured electric or magnetic field, one must take into account that the derivative along the flow direction (x axis) cannot be neglected with respect to the derivative along the thickness (z axis) as commonly assumed [17,22]. In fact, we have shown that there are regions of the cell, in particular close to the stepwise discontinuity, where the physical scenario is quite in disagreement with classical lubrication assumptions. This behavior has to be taken into account in any coherent theory of lubrication that involves nematics, which will be the subject of a dedicated contribution.

Finally, we stress that our model is expected to quantitatively fail in its application to geometries that exhibit edges or to nematic cells whose thickness is comparable with the nematic coherence length (of the order of few tens of nanometres). In these limits, as discussed in Ref. [23], the confinement can induce biaxiality, thus the Frank model cannot be applied to. However, the latter scenario can be predicted recurring to the Landau-de Gennes theory for nematics.

[1] M. Scaraggi, Phys. Rev. E **86**, 026314 (2012); Proc. R. Soc. A **471**, 20140739 (2015).
[2] M. Scaraggi, Tribol. Lett. **48**, 375 (2012).
[3] M. Scaraggi, Tribol. Lett. **53**, 127 (2014).
[4] M. Scaraggi, Proc. Inst. Mech. Eng., Part J **229**, 493 (2015).
[5] E. G. Virga, *Variational Theories for Liquid Crystals* (Chapman and Hall, London, 1995).
[6] I. W. Stewart, *The Static and Dynamic Continuum Theory of Liquid Crystals: A Mathematical Introduction* (Taylor & Francis, London/New York, 2004).
[7] F. Lonberg and R. B. Meyer, Phys. Rev. Lett. **55**, 718 (1985).
[8] G. Bevilacqua and G. Napoli, Phys. Rev. E **81**, 031707 (2010).
[9] G. Napoli, Europhys. Lett. **92**, 46006 (2010).
[10] A. Sparavigna, O. D. Lavrentovich, and A. Strigazzi, Phys. Rev. E **49**, 1344 (1994).
[11] S. Kralj, R. Rosso, and E. G. Virga, Eur. Phys. J. E **17**, 37 (2005).
[12] A. L. Alexe-Ionescu, G. Barbero, and I. Lelidis, Phys. Rev. E **66**, 061705 (2002).
[13] T. Shioda, B. Wen, and C. Rosenblatt, J. Appl. Phys. **94**, 7502 (2003).
[14] K. Nakano, Tribol. Lett. **14**, 17 (2003).
[15] M. De Volder, K. Yoshida, S. Yokota, and D. Reynaerts, J. Micromech. Microeng. **16**, 612 (2006).
[16] M. Cidade, G. Pereira, A. Bubnov, V. Hamplova, M. Kaspar, and J. Casquilho, Liquid Cryst. **39**, 191 (2012).
[17] J. A. Tichy, Tribol. Trans. **33**, 363 (1990).
[18] G. Napoli and S. Turzi, Comput. Math. Appl. **55**, 299 (2008).
[19] R. H. Self, C. Please, and T. J. Sluckin, Eur. J. Appl. Math. **13**, 1 (2002).
[20] G. Napoli, J. Phys. A: Math. Gen. **39**, 11 (2006).
[21] W. Winslow, J. Appl. Phys. **20**, 1137 (1949).
[22] M. Ben Amar and L. J. Cummings, Phys. Fluids **13**, 1160 (2001).
[23] S. Kralj and A. Majumdar, Proc. R. Soc. London A **470**, 2169 (2014).
[24] The shown numerical results are from three simulations performed at (geometrically) increasing refinement, thus showing that numerical convergence is achieved.